

1  
2 **MESSENGER Observations of Standing Whistler Waves Upstream of Bow Shock of**  
3 **Mercury**

4 **Yang Wang<sup>1,2</sup>, Jun Zhong<sup>1,2</sup>, James Slavin<sup>3</sup>, Hui Zhang<sup>1,2</sup>, Lou-Chuang Lee<sup>4,5</sup>, Lican**  
5 **Shan<sup>1,2</sup>, Yong Wei<sup>1,2</sup>, Yongxin Pan<sup>1,2</sup>**

6 <sup>1</sup>Key Laboratory of Earth and Planetary Physics, Institute of Geology and Geophysics, Chinese  
7 Academy of Sciences, Beijing, China

8 <sup>2</sup>College of Earth and Planetary Sciences, University of Chinese Academy of Sciences, Beijing,  
9 China

10 <sup>3</sup>Department of Climate and Space Sciences and Engineering, University of Michigan, Ann  
11 Arbor, Michigan, USA

12 <sup>4</sup>Institute of Earth Sciences, Academia Sinica, Taipei, Taiwan

13 <sup>5</sup>State Key Laboratory of Lunar and Planetary Sciences, Macau University of Science and  
14 Technology, Macau, China

15 Correspondence to: Jun Zhong (j.zhong@mail.iggcas.ac.cn)

16 **Key Points:**

- 17 • We identify 36 Mercury's bow shock crossings with standing whistler waves during  
18 interplanetary coronal mass ejection intervals.
- 19 • The amplitude, polarization, and damping length of the standing whistler waves were  
20 identified and statistically analyzed.
- 21 • These standing whistler waves may be generated by currents in shock, and the shock is  
22 not the largest-amplitude circle of the waves.

## 23 **Abstract**

24 This paper reports on the standing whistler waves upstream of Mercury's quasi-perpendicular  
25 bow shock. Using MESSENGER's magnetometer data, 36 wave events were identified during  
26 interplanetary coronal mass ejections (ICMEs). These elliptic or circular polarized waves were  
27 characterized by: (1) a constant phase with respect to the shock, (2) propagation along the normal  
28 direction to the shock surface, and (3) rapid damping over a few wave periods. We inferred the  
29 speed of Mercury's bow shock as  $\sim 31$  km/s and a shock width of 1.76 ion inertial length. These  
30 events were observed in 20% of the MESSENGER orbits during ICMEs. We conclude that  
31 standing whistler wave generations at Mercury are generic to ICME impacts and the low Alfvén  
32 Mach number ( $M_A$ ) collisionless shock, and are not affected by the absolute dimensions of its  
33 bow shock. Our results further support the theory that these waves are generated by the current in  
34 the shock.

## 35 **Plain Language Summary**

36 The strength of planetary bow shocks varies with the planet's heliocentric distance from the Sun.  
37 Studying the bow shocks of other planets is important for extending our understanding of  
38 collisionless-shock physics. In the solar system, the bow shocks of Mercury are unique as they  
39 are produced by low Mach numbers and low plasma beta solar wind blowing over a small  
40 magnetized body that is 1–2 orders smaller than Earth. The standing whistler waves upstream of  
41 the bow shock of Mercury were determined through statistical analyses. Similar to the  
42 observations at Earth, these waves were rapidly damping with a proportion of the wave periods;  
43 however, the damping distance at the spacecraft frame was considerably shorter at only a few  
44 kilometers upstream in the small-scale bow shock of Mercury. The high occurrence rate of  
45 standing whistler waves suggests that Mercury's bow shock is a natural plasma laboratory, which  
46 can be used to further investigate low  $M_A$  planetary shocks during the upcoming BepiColombo  
47 mission.

## 48 **1 Introduction**

49 Whistler waves are common upstream features of planetary bow shocks and are involved  
50 in shock formation and particle interactions (Balogh et al., 2013; Oka et al., 2017; Oka et al.,  
51 2019). Two types of whistler waves emitting from shock ramps have been previously identified:  
52 propagating and phase standing (Russell et al., 1995). The propagation direction of propagating

53 whistler waves has a small angle with the magnetic field and they propagate far upstream  
54 (Russell et al., 2007). They have been widely observed upstream of the bow shock of Earth and  
55 are typically called “1 Hz” waves. Furthermore, they are also commonly observed in other  
56 planetary shocks, such as those of Mercury, Venus, Mars, and Saturn (Fairfield et al., 1976;  
57 Orłowski et al., 1991; Le et al., 2013; Sulaiman et al., 2017; Ruhunusiri et al., 2018). In contrast,  
58 phase standing whistler waves are generated when the wave propagation speed equals the  
59 component of the solar wind velocity that is normal to the bow shock (Perez et al., 1970). They  
60 propagate along the shock-normal direction at a constant phase with respect to the shock ramp  
61 and can rapidly damp within a few wave periods. The right-handed wave polarization relative to  
62 its average field direction is a key observational feature, when an observer moves upstream to  
63 downstream. In contrast, the left-handed wave polarization can be observed when the observer  
64 moves in the opposite direction. Standing whistler waves have been rarely observed upstream of  
65 the bow shock of the Earth (e.g., Fairfield et al., 1975; Mellott et al., 1984; Farris et al., 1993) as  
66 they commonly occur under low  $M_A$  conditions, such as during an ICME passage.

67 Mercury has a miniature and weak bow shock, which is created by the interaction of low  
68 Mach number solar wind and a relatively small planetary magnetosphere in the inner  
69 hemisphere. The average bow shock subsolar distance has been determined to be only  $\sim 2 R_M$   
70 (radius of Mercury,  $1 R_M = 2440$  km), which is approximately 1–2 orders smaller than that of the  
71 Earth (Winslow et al., 2013). The “1 Hz” whistler waves have been commonly observed  
72 upstream of the bow shock of Mercury (Fairfield et al., 1976; Le et al., 2013), in which they  
73 propagate along the magnetic field and farther upstream ( $\sim 30000$  km). Although phase standing  
74 whistler waves have been observed at Mercury, they have not yet been analyzed (Gedalin et al.,  
75 2022).

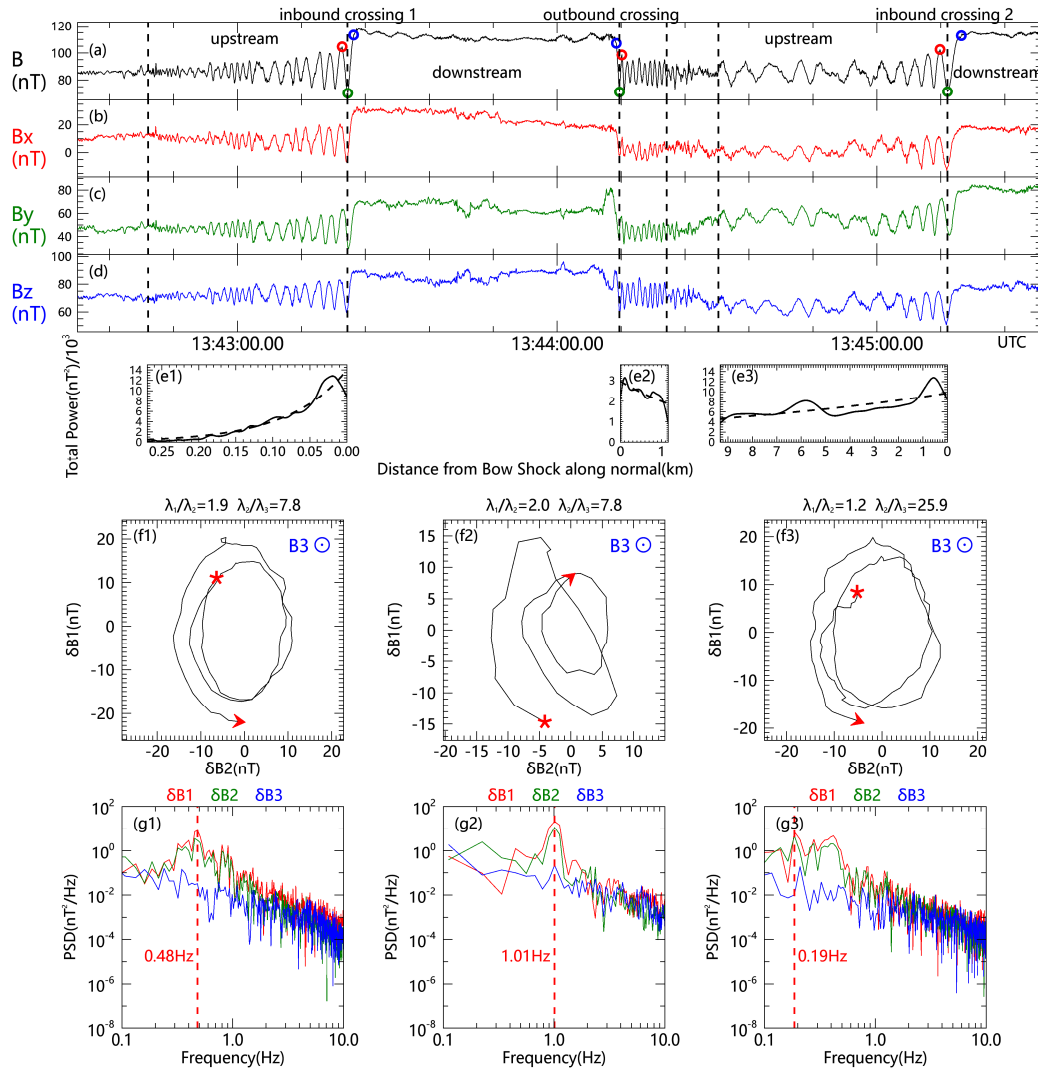
76 Due to the nature of close-in orbit, there is higher probability for observing low  $M_A$   
77 shocks at Mercury than other planets. The typical  $M_A$  at Mercury orbit is  $\sim 4$ –6 (Slavin et al.,  
78 1981). Especially, the  $M_A$  can be less than 3 during ICMEs (Liu et al., 2005; Sarantos et al.,  
79 2009). The ICME impact on Mercury’s magnetosphere was first analyzed by Slavin et al. (2014).  
80 They showed that Mercury’s dayside magnetosphere is highly dynamic and greatly compressed  
81 by ICME impacts. The bow shock and magnetopause reconfigurations during the impact of  
82 ICMEs deviates greatly from normal conditions (Slavin et al., 2014; Winslow et al., 2015;  
83 2017), and the dayside magnetosphere may even occasionally disappeared (Slavin et al., 2019;

84 Winslow et al., 2020). MESSENGER orbited Mercury during the maximum of solar cycle 24.  
85 Over the four-year mission from February 2011 to April 2015, a total of 69 ICMEs were detected  
86 by MESSENGER (Winslow et al. 2015, 2017). We use the 69 ICMEs to study standing whistler  
87 waves.

88 Here we report the MESSENGER observations of the standing whistler wave upstream  
89 Mercury's bow shock during ICMEs collated by Winslow et al. (2015, 2017). Among 69 ICMEs,  
90 we identified 36 standing whistler wave events corresponding to at least 20% of the orbits. Our  
91 results suggest that Mercury is a natural plasma laboratory for the understand the physics of  
92 standing whistler waves and low  $M_A$  collisionless shocks. It is likely that our understanding of  
93 such low Mach number shocks will be greatly advanced by measurements to be collected by the  
94 upcoming Bepi-Colombo mission.

## 95 **2 Case Analysis of Standing Whistler Wave**

96 The dynamics of dayside magnetosphere and magnetotail response to an ICME observed  
97 by MESSENGER on November 23, 2011 have been analyzed in detail by Slavin et al. (2014)  
98 and Zhong et al. (2020), respectively. This study analyzes its effects on the bow shock. Figures  
99 1a–d show an overview of MESSENGER's bow shock crossings during this ICME. High-  
100 resolution magnetic field data (20 vectors  $s^{-1}$ ) obtained from the magnetometer (MAG; Anderson  
101 et al., 2007) were used and displayed in the aberrated Mercury solar magnetic (MSM)  
102 coordinates. The MSM coordinate system was centered on the offset internal dipole of Mercury  
103 (Anderson et al., 2011), wherein the X-axis was pointed toward the Sun, the Y-axis was pointed  
104 in the opposite direction of the orbit motion, and the Z-axis completed the right-handed system.  
105 The average radial solar wind speed of  $700 \text{ km s}^{-1}$  during the ICME was applied to correct for the  
106 aberration. The spacecraft crossed the bow shock thrice; the crossings are denoted as inbound  
107 crossing 1, outbound crossing, and inbound crossing 2 in Figure 1. The multiple crossings may  
108 be attributed to the temporal variations of the upstream solar wind conditions.



109

110 **Figure 1.** MESSANGER observations of standing whistler waves upstream of the bow shock of  
 111 Mercury during the ICME on 23 November 2011. **(a)–(d)** Magnetic field strength and its three  
 112 components in the aberrated MSM coordinate system; the red, green, and blue dots correspond to  
 113 the peak, wave trough, and end of the shock ramp, respectively. **(e)** Total power as a function of  
 114 the distance from the bow shock along shock normal. **(f)–(g)** Magnetic field data of the wave in  
 115 the maximum-intermediate plane and the power spectral density in the minimum variance  
 116 analysis (MVA) after removing the background magnetic field. The  $T_{\text{ramp}}$  refers to the interval  
 117 time between the blue and green dots. The  $T_{\text{wave}}$  refers to twice the interval time between the red  
 118 and green dots.

119 The shock normal was determined using the magnetic coplanarity method (Lepping et al.,  
 120 1971) that substitutes the average magnetic field upstream and downstream of the shock; it is  
 121 expressed as  $\mathbf{n} = \frac{(\mathbf{B}_1 \times \mathbf{B}_2) \times (\mathbf{B}_2 - \mathbf{B}_1)}{|(\mathbf{B}_1 \times \mathbf{B}_2) \times (\mathbf{B}_2 - \mathbf{B}_1)|}$ . The shock normals for the inbound  
 122 crossing, and inbound crossing 2 were observed to be very close at (0.56, -0.05, -0.82), (0.71, -

123 0.02, -0.70), and (0.76, -0.06, -0.65), respectively, and their mean upstream magnetic fields were  
 124 (9.24, 46.57, 72.37), (2.40, 45.41, 71.94), and (1.33, 55.94, 64.86) nT, respectively. The angles  
 125 between the mean upstream magnetic field  $\mathbf{B}_{\text{up}}$  and the shock normal  $\mathbf{n}$  were  $\theta_{\text{Bn}} = 49.13^\circ$ ,  
 126  $52.23^\circ$ , and  $58.49^\circ$ , indicating quasi-perpendicular shocks.

127 The accompanying upstream waves are considered key features of these bow shock  
 128 crossings. The polarizations and vectors of these waves were obtained from the results of the  
 129 minimum variance analysis (MVA) of the magnetic field within an upstream wave time interval  
 130 (Sonnerup et al., 1967). Using these, the direction of propagation for an assumed planar wave  
 131 can be estimated. For inbound crossing 1, the small ratio of the maximum to intermediate  
 132 eigenvalues  $\lambda_1/\lambda_2 = 1.9$  and the large ratio of the intermediate to minimum eigenvalues  $\lambda_2/\lambda_3 =$   
 133  $7.8$  suggest that the waves had relatively stable elliptic polarizations. The wave vector  $\mathbf{k}$   
 134 corresponds to the minimum variance eigenvector  $\mathbf{e}_3$  (0.70, -0.11, -0.69), whereas the  
 135 corresponding mean magnetic field ( $\mathbf{B}_0$ ) is directed out of the maximum-intermediate plane. The  
 136 hodograms of the magnetic field for several wavelengths in the MVA coordinates are shown in  
 137 Figure 1f. The gyration of the magnetic field with respect to  $\mathbf{B}_0$  indicates that the wave  
 138 polarization was right-handed in the spacecraft coordinate frame (SCF). The angles between  $\mathbf{k}$   
 139 and  $\mathbf{n}$  ( $\theta_{\text{kn}}$ ) and  $\mathbf{k}$  and  $\mathbf{B}_{\text{up}}$  ( $\theta_{\text{kB}}$ ) were  $11.85^\circ$  and  $55.49^\circ$ , respectively, wherein the small  $\theta_{\text{kn}}$  and  
 140 large  $\theta_{\text{kB}}$  suggest that the wave propagated approximately along the shock normal direction  
 141 rather than the magnetic field.

142 The waves observed during the outbound crossing and inbound crossing 2 were also  
 143 elliptically polarized (Figures 1f2 and f3), with  $\theta_{\text{kn}} = 23.18^\circ$ ,  $2.82^\circ$  and  $\theta_{\text{kB}} = 64.17^\circ$ ,  $58.14^\circ$ ,  
 144 respectively. Moreover, the polarization direction of the outbound crossing was opposite to that  
 145 of the inbound crossing, wherein it was left-handed, which is consistent with the characteristics  
 146 of standing whistler waves (Fairfield et al., 1975; Mellott et al., 1984).

147 Wavelet analysis was used to calculate the total power at each moment. Figure 1e shows  
 148 the variations of the total power along  $\mathbf{n}$  in the SCF. The function  $P = P_0 e^{-T/T_0}$  was fit to the total  
 149 power. For inbound crossing 1, the damping time ( $T_0$ ) was 11.17 s, which was 5.32 times the  
 150 wave period ( $T_{\text{wave}}$ ), indicating rapid damping. The damping distance was 1.83 km along  $\mathbf{k}$  and  
 151 the normalized wave amplitude ( $\delta B_{\text{wave}}/B_u$ ) was 0.40. This rapid damping of waves was also  
 152 observed during the outbound crossing and inbound crossing 2.

153 The power spectral density shown in Figure 1e demonstrates that these waves were  
 154 mainly restricted to the plane perpendicular to  $\mathbf{e}_3$ , as indicated by the  $\text{PSD}_1$ , and  $\text{PSD}_2 \gg \text{PSD}_3$   
 155 around the wave frequency ( $f_{\text{sc}}$ ) in the SCF. The  $f_{\text{sc}}$  for the inbound crossing 1, outbound  
 156 crossing, and inbound crossing 2 were  $\sim 0.48$ ,  $1.01$ , and  $0.19$  Hz, respectively; the different  
 157 values indicate the change in the relative velocity between the spacecraft and bow shock in the  
 158 normal direction.

### 159 **3 Statistical Results and Discussion**

#### 160 **3.1 Statistical Results**

161 We use 69 ICMEs (94 orbits) collated by Winslow et al. (2015, 2017) to find bow shock  
 162 crossings during ICMEs. As standing whistler waves typically occur upstream of the quasi-  
 163 perpendicular bow shock, the  $\theta_{\text{Bn}}$  was calculated, wherein 486 quasi-perpendicular bow shock  
 164 crossings ( $\theta_{\text{Bn}} > 45^\circ$ ) were identified to select the events. Multiple bow shock crossings are  
 165 common during inbound or outbound crossings in each orbit owing to the up-and-down  
 166 displacement of the shocks. MVA was performed on the magnetic field data upstream for each  
 167 quasi-perpendicular shock crossing under the assumption that the eigenvalues conform to  $\lambda_1/\lambda_2 <$   
 168  $2$  and  $\lambda_2/\lambda_3 > 7$ , which indicate that the waves are elliptically or circularly polarized. In all  
 169 elliptically polarized waves, 36 perpendicular bow shock crossings with rapid damping were  
 170 identified, including 20 inbound and 16 outbound crossings. They occurred during 19 orbits,  
 171 with an orbital occurrence rate of  $\sim 20\%$ .

172 The characteristics of the wave during each event were observed (Supplement Table 1).  
 173 A statistical analysis indicated the following:

174 *Wave polarization.* Right-handed polarization was observed in 16 of the 20 upstream to  
 175 downstream traversals, whereas left-handed polarization was observed in all 16 downstream to  
 176 upstream traversals. These polarizations were consistent with the previous theory and  
 177 observation of standing whistler waves presented by Perez et al. (1970) and Fairfield et al.  
 178 (1975).

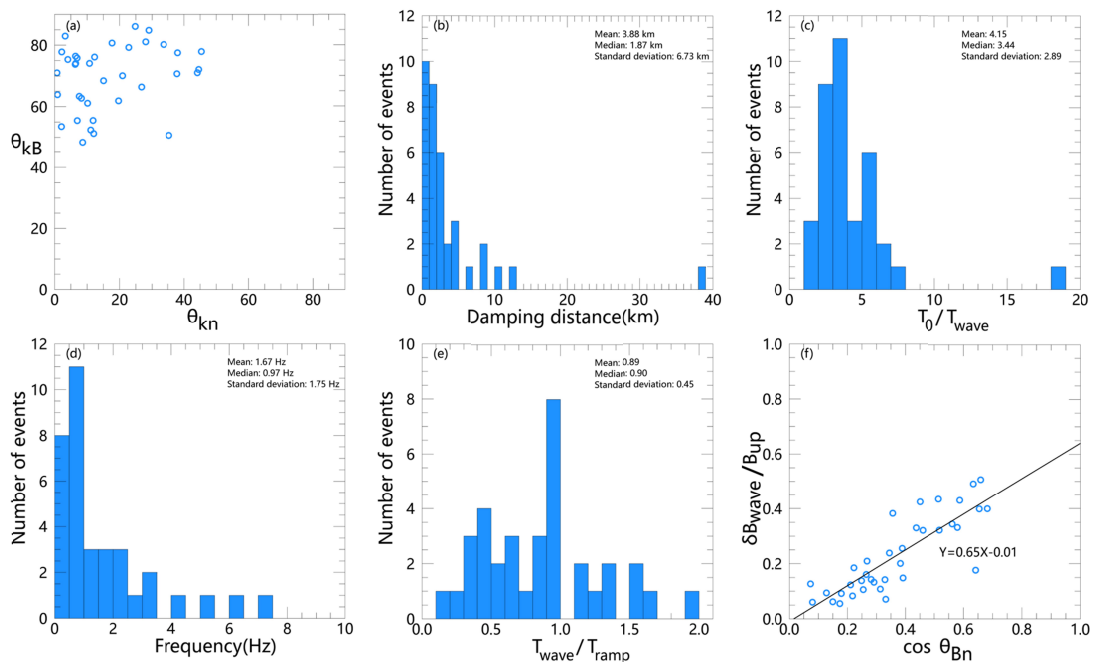
179 *Propagation direction.* The calculated  $\theta_{\text{kn}}$  ranged from  $\sim 0^\circ$  to  $50^\circ$ , while the  $\theta_{\text{kB}}$  ranged  
 180 from  $\sim 45^\circ$  to  $90^\circ$  (Figure 2a). The mean  $\theta_{\text{kn}}$  and  $\theta_{\text{kB}}$  were  $17.31^\circ$  and  $69.55^\circ$ , respectively. These  
 181 results suggest that the waves were propagating along the shock normal instead of the magnetic

182 field. These results are also consistent with the observations at Earth (Mellott et al., 1984);  
 183 however, they are different from the propagating direction of “1 Hz” waves observed at Mercury  
 184 (Fairfield et al., 1976; Le et al., 2013).

185 *Wave damping.* Figure 2b shows the distance from the wave damping to  $e^{-1}$  to the ramp  
 186 on the  $\mathbf{n}$  in the SCF, wherein the amplitudes of most waves damp at  $e^{-1}$  within 10 km. This was  
 187 significantly less than the damping distance of the “1 Hz” wave within  $\sim 30000$  km at Mercury  
 188 (Le et al., 2013). The ratio of  $T_0$  and  $T_{\text{wave}}$  was nearly  $<10$  (Figure 2c). The standing whistler  
 189 waves on Earth also exhibit this rapid damping, which is  $<10$  times the wave periods (Mellott et  
 190 al., 1984); hence, the damping mechanism can be considered as Landau damping (Gary et al.,  
 191 1985).

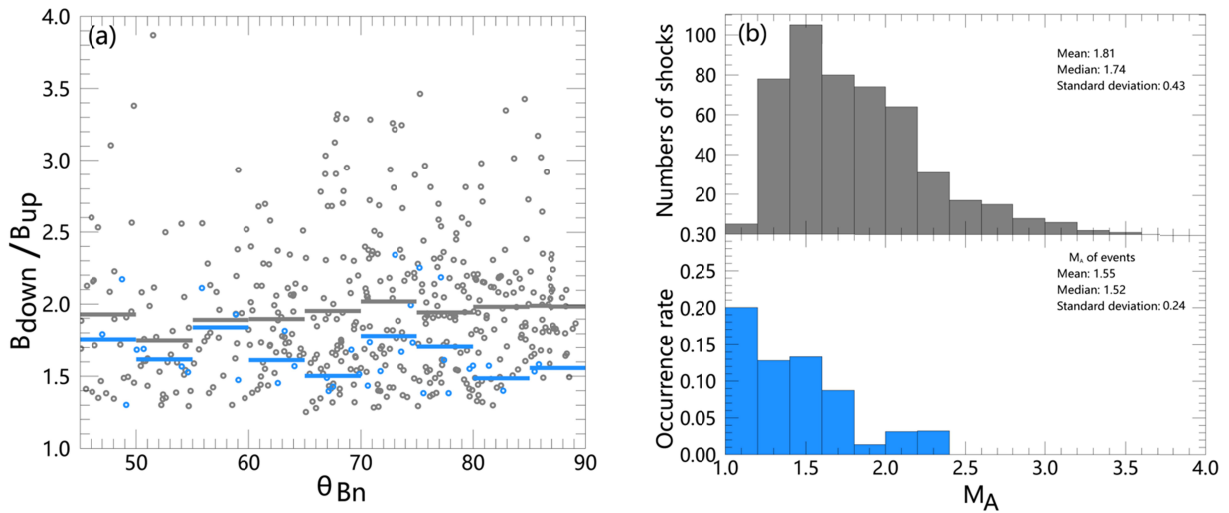
192 *Wave frequency.* The mean frequency of standing whistler waves was 1.67 Hz in the  
 193 SCF. Here, 70% of the events had a frequency  $<2$  Hz (Figure 2d), suggesting that the standing  
 194 whistler waves have a lower frequency than the “1 Hz” waves at Mercury (2–3 Hz, Russell,  
 195 2007).

196 Based on the statistical results of these events, it was discovered that its characteristics  
 197 were similar with those of the standing whistler wave. Meanwhile, other properties (Figures 2e  
 198 and f) of the waves are described in detail in the Discussion Section.



200 **Figure 2.** Statistical properties of the standing whistler waves upstream of the bow shock of  
 201 Mercury. **(a)** Occurrence of events as functions of  $\theta_{kn}$  and  $\theta_{kB}$ . **(b)–(e)** Distributions of damping  
 202 distance,  $T_0/T_{wave}$ , frequency, and  $T_{wave}/T_{ramp}$ . **(f)** Correlation between  $\theta_{Bn}$  and  $\delta B_{wave}/B_{up}$ .

203 Considering that the solar wind beam view of MESSENGER's fast imaging plasma  
 204 spectrometer was obstructed by the sunshade, the upstream solar wind  $M_A$  could not deviate  
 205 directly. The  $M_A$  was approximatively estimated using the following formula:  $M_A - 1 =$   
 206  $(B_{down}/B_{up} - 1) \sin^2 \theta_{Bn}$ , which is suitable for low Mach number and low- $\beta$  shocks. (Balikhin et  
 207 al., 2008). The magnetic field compression ratio ( $B_{down}/B_{up}$ : magnetic field intensity (average  
 208 value of  $\sim 1$  min) ratio of downstream to upstream) of all perpendicular bow shock crossings  
 209 during ICMEs are plotted in Figure 3a, wherein it can be observed that most of the identified  
 210 wave events (blue) had lower magnetic field compression ratios than the mean ratio during  
 211 ICMEs. The distributions of the calculated  $M_A$  and wave event occurrence rates are plotted in  
 212 Figure 3b, wherein the occurrence rate can be observed to increase as  $M_A$  decreases; 89% of the  
 213 wave events obtained lower  $M_A$  values than the average value during ICMEs. Therefore, these  
 214 waves have a high likelihood of occurrence under a relatively lower Mach number.



215

216 **Figure 3. (a)** Variations of the magnetic field compression ratio with  $\theta_{Bn}$ . The gray and blue  
 217 lines represent the average values of all shocks and wave events, respectively. **(b)** Distributions  
 218 of  $M_A$  (top) and events occurrence rates (bottom; Unit : Number of events/Number of shocks in  
 219 each  $M_A$  bin).

### 220 3.2 Discussion

221 On Earth, the theoretical wavelengths of standing whistler waves are consistent with  
 222 those observed by Mellott et al. (1984). Hence, single spacecraft observations are normally used

223 to infer the bow shock speed (Fairfield et al., 1975) based on theoretical predictions of the  
 224 wavelength (Tidman et al., 1971):  $\lambda = \frac{2\pi c \cos\theta_{BN}}{\omega_{pi}(M_A^2 - 1)^{1/2}}$ , where  $\omega_{pi}$  is the proton plasma frequency.  
 225 By applying the typical values from the ICME model at 0.38 AU (Liu et al., 2005),  $\omega_{pi} =$   
 226  $10034 \text{ rad/s}$ , mean  $M_A = 1.55$ , and mean  $\theta_{BN} = 68^\circ$  of all wave events, the theoretically  
 227 predicted wavelength of  $\lambda = \sim 59 \text{ km}$  was calculated. The average  $T_{\text{wave}}$  was  $\sim 1.89 \text{ s}$ ; hence, the  
 228 shock speed ( $\lambda/T_{\text{wave}}$ ) can be inferred as  $\sim 31 \text{ km/s}$ . Notably, this was slightly less than the shock  
 229 speed of  $\sim 40 \text{ km/s}$  estimated through overshoot observations under normal conditions (Masters  
 230 et al., 2015).

231 The shock ramp scale was also estimated using the scale relationship between the  
 232 standing whistler waves and the shock ramps. A shock ramp scale of 53 km was obtained using  
 233 the formula  $\lambda \times T_{\text{ramp}}/T_{\text{wave}}$  ( $59 \text{ km} \times 0.89$ ). Considering an ion inertial length ( $c/\omega_{pi}$ ) of 30 km,  
 234 the width of the ramp was  $1.76 c/\omega_{pi}$ . Based on the results of Hobara et al. (2010), the scale can  
 235 be larger than  $1 c/\omega_{pi}$  when  $M_A$  is low.

236 Previous theories have suggested that standing whistler waves are generated by a stable  
 237 current in the shock ramp, from which the formula for the wave amplitude can be derived  
 238 (Tidman et al., 1971). This theory suggests that  $\delta B_{\text{wave}}/B_{\text{up}}$  has a positive correlation with  $\cos\theta_{BN}$ ,  
 239 and this relationship is demonstrated in Figure 2f. The best linear fit produced  $Y = [0.65 \pm 0.15]X$   
 240  $- [0.01 \pm 0.06]$ , which was also consistent with this theory. Based on the fitted values, the  
 241 maximum amplitude of the standing whistler wave was approximately 0.8 times the intensity of  
 242 the background magnetic field.

243 The shock is hypothesized to be the largest-amplitude circle of the upstream standing  
 244 whistler wave, wherein its width is half of the wavelength. However, this results in conflicting  
 245 ratios of the standing whistler wave wavelength to the shock thickness at Earth and  
 246 interplanetary shock, as some researchers have estimated this ratio to be two (Goncharov et al.,  
 247 2014) while others have estimated it to be closer to one (Mellott et al., 1984; Farris et al., 1993).  
 248 In the SCF, the ratio between the period ( $T_{\text{wave}}$ ) of the upstream whistler waves and the shock  
 249 ramp crossing time ( $T_{\text{ramp}}$ ) can be a good approximation of the shock width to wavelength ratio.  
 250 Figure 2e shows the  $T_{\text{wave}}/T_{\text{ramp}}$  in the spacecraft frame of the upstream standing whistler waves  
 251 of Mercury. In cases where  $T_{\text{wave}}$  was less than  $2 \times T_{\text{ramp}}$ , the average ratio of the two was 0.89,

252 indicating that the initial hypothesis must be reexamined to further determine the scale of the  
253 relationship between standing whistler waves and shock ramps.

#### 254 **4 Conclusions**

255 In this study, we reported and statistically analyzed the standing whistler waves upstream  
256 of the bow shock of Mercury during ICMEs. These waves occur at lower  $M_A$  and propagate  
257 along the normal of the bow shock. It was observed that, similar to the waves at Earth, these  
258 waves were rapidly damping with few wave periods; however, the damping distance in SCF was  
259 significantly shorter, only a few kilometers upstream of the bow shock of Mercury. Our results  
260 support that these waves are generated by the current in the shock and that the shock is not the  
261 largest-amplitude circle of the waves. Hence, the generation of standing whistler waves was  
262 determined to be generic to the low Mach number collisionless shock. Additionally, a high  
263 occurrence rate of the standing whistler waves observed during ICMEs suggests that the bow  
264 shock of Mercury can be a natural plasma laboratory that can be used to further study low  $M_A$   
265 planetary shocks. Considering that BepiColombo will arrive at Mercury in 2025 during the  
266 ascending and maximum phases of solar cycle 25, it is expected to encounter a large number of  
267 ICMEs. This study provides an understanding of standing whistler wave generation and their  
268 underlying physics, which can be used for the upcoming high-resolution BepiColombo  
269 observations.

#### 270 **Acknowledgments**

271 This work was supported by the National Natural Science Foundation of China (41621004), and  
272 the Key Research Program of the Institute of Geology & Geophysics, CAS (Grant No. IGGCAS-  
273 201904 and IGGCAS-202102). J. A. Slavin acknowledges support from NASA grants  
274 80NSSC18K1137, 80NSSC21M0364 and 80NSSC21K0052. L. C. Lee was supported by the  
275 Science and Technology Development Fund (FDCT) of Macau (0035/2018/AFJ) and the  
276 Ministry of Science and Technology, Taiwan (MOST 110-2111-M-002-017). MESSENGER  
277 data are available from the Planetary Data System (MAG).

#### 278 **Open Research**

279 The MESSENGER MAG data used in this study are available at NASA's Planetary Data  
280 System:

281 <https://pds-ppi.igpp.ucla.edu/search/view/?f=yes&id=pds://PPI/mess-mag-calibrated/data/mso;>

282 The list of the identified standing whistler wave events is available in the supplemental  
283 information for the purposes of peer review. The data will eventually be deposited at NSSDC  
284 Space Science Article Data Repository (<https://sadr-en.nssdc.ac.cn>) by the time it is accepted.

## 285 References

- 286 Anderson, B. J., Acuña, M. H., Lohr, D. A., Scheifele, J., Raval, A., Korth, H., & Slavin, J. A. (2  
287 007). The Magnetometer instrument on MESSENGER. In *The MESSENGER mission to Merc*  
288 *ury* (pp. 417-450). Springer, New York, NY. <https://doi.org/10.1007/s11214-007-9246-7>
- 289 Anderson, B. J., Johnson, C. L., Korth, H., Purucker, M. E., Winslow, R. M., Slavin, J. A., ... &  
290 Zurbuchen, T. H. (2011). The global magnetic field of Mercury from MESSENGER orbital ob  
291 servations. *Science*, 333(6051), 1859-1862. <https://doi.org/10.1126/science.1211001>
- 292 Balikhin, M. A., Zhang, T. L., Gedalin, M., Ganushkina, N. Y., & Pope, S. A. (2008). Venus Exp  
293 ress observes a new type of shock with pure kinematic relaxation. *Geophysical Research Lette*  
294 *rs*, 35(1). <https://doi.org/10.1029/2007GL032495>
- 295 Balogh, A., & Treumann, R. A. (2013). *Physics of collisionless shocks: space plasma shock wav*  
296 *es*. Springer Science & Business Media.
- 297 Fairfield, D. H., & Feldman, W. C. (1975). Standing waves at low Mach number laminar bow sh  
298 ocks. *Journal of Geophysical Research*, 80(4), 515-522. <https://doi.org/10.1029/JA080i004p0>  
299 0515
- 300 Fairfield, D. H., & Behannon, K. W. (1976). Bow shock and magnetosheath waves at Mercury. *J*  
301 *ournal of Geophysical Research*, 81(22), 3897-3906. <https://doi.org/10.1029/JA081i022p0389>  
302 7
- 303 Farris, M. H., Russell, C. T., & Thomsen, M. F. (1993). Magnetic structure of the low beta, quasi  
304 -perpendicular shock. *Journal of Geophysical Research: Space Physics*, 98(A9), 15285-15294  
305 . <https://doi.org/10.1029/93JA00958>
- 306 Gary, S. P., & Mellott, M. M. (1985). Whistler damping at oblique propagation: Laminar shock p  
307 recursors. *Journal of Geophysical Research: Space Physics*, 90(A1), 99-104. <https://doi.org/10>  
308 [.1029/JA090iA01p00099](https://doi.org/10.1029/JA090iA01p00099)
- 309 Gedalin, M., Golbraikh, E., Russell, C. T., & Dimmock, A. P. (2022). Theory helps observations:  
310 determination of the shock mach number and scales from magnetic measurements. *Frontiers i*  
311 *n Physics*, 149. <https://doi.org/10.3389/fphy.2022.852720>
- 312 Greenstadt, E. W., Russell, C. T., Scarf, F. L., Formisano, V., & Neugebauer, M. (1975). Structu  
313 re of the quasi-perpendicular laminar bow shock. *Journal of Geophysical Research*, 80(4), 502  
314 -514. <https://doi.org/10.1029/JA080i004p00502>

- 315 Goncharov, O., Šafránková, J., Němeček, Z., Přeč, L., Pitňa, A., & Zastenker, G. N. (2014). Up  
316 stream and downstream wave packets associated with low-Mach number interplanetary shock  
317 s. *Geophysical Research Letters*, *41*(22), 8100-8106. <https://doi.org/10.1002/2014GL062149>
- 318 Hobara, Y., Balikhin, M., Krasnoselskikh, V., Gedalin, M., & Yamagishi, H. (2010). Statistical s  
319 tudy of the quasi - perpendicular shock ramp widths. *Journal of Geophysical Research: Space*  
320 *Physics*, *115*(A11). <https://doi.org/10.1029/2010JA015659>
- 321 Kennel, C. F. (1994, August). The magnetohydrodynamic Rankine-Hugoniot relations. In *AIP C*  
322 *onference Proceedings* (Vol. 314, No. 1, pp. 180-227). American Institute of Physics. <https://doi.org/10.1063/1.46750>
- 324 Liu, Y., Richardson, J. D., & Belcher, J. W. (2005). A statistical study of the properties of interpl  
325 anetary coronal mass ejections from 0.3 to 5.4 AU. *Planetary and Space Science*, *53*(1-3), 3-1  
326 7. <https://doi.org/10.1016/j.pss.2004.09.023>
- 327 Lepping, R. P., & Argentiero, P. D. (1971). Single spacecraft method of estimating shock normal  
328 s. *Journal of Geophysical Research*, *76*(19), 4349-4359. [https://doi.org/10.1029/JA076i019p0](https://doi.org/10.1029/JA076i019p04349)  
329 4349
- 330 Le, G., Chi, P. J., Blanco-Cano, X., Boardsen, S., Slavin, J. A., Anderson, B. J., & Korth, H. (20  
331 13). Upstream ultra-low frequency waves in Mercury's foreshock region: MESSENGER magn  
332 etic field observations. *Journal of Geophysical Research: Space Physics*, *118*(6), 2809-2823. <https://doi.org/10.1002/jgra.50342>
- 334 Masters, A., Slavin, J. A., DiBraccio, G. A., Sundberg, T., Winslow, R. M., Johnson, C. L., ... &  
335 Korth, H. (2013). A comparison of magnetic overshoots at the bow shocks of Mercury and Sat  
336 urn. *Journal of Geophysical Research: Space Physics*, *118*(7), 4381-4390. [https://doi.org/10.1](https://doi.org/10.1002/jgra.50428)  
337 002/jgra.50428
- 338 Mellott, M. M., & Greenstadt, E. W. (1984). The structure of oblique subcritical bow shocks: IS  
339 EE 1 and 2 observations. *Journal of Geophysical Research: Space Physics*, *89*(A4), 2151-216  
340 1. <https://doi.org/10.1029/JA089iA04p02151>
- 341 Oka, M., Wilson III, L. B., Phan, T. D., Hull, A. J., Amano, T., Hoshino, M., ... & Lindqvist, P.  
342 A. (2017). Electron scattering by high-frequency whistler waves at earth's bow shock. *The Ast*  
343 *rophysical Journal Letters*, *842*(2), L11. <https://doi.org/10.3847/2041-8213/aa7759>
- 344 Oka, M., Otsuka, F., Matsukiyo, S., Wilson, L. B., Argall, M. R., Amano, T., ... & Lindqvist, P.  
345 A. (2019). Electron scattering by low-frequency Whistler waves at Earth's bow shock. *The Ast*  
346 *rophysical Journal*, *886*(1), 53. <https://doi.org/10.3847/1538-4357/ab4a81>
- 347 Orłowski, D. S., & Russell, C. T. (1991). Ulf waves upstream of the Venus bow shock: Propertie  
348 s of one-hertz waves. *Journal of Geophysical Research: Space Physics*, *96*(A7), 11271-11282  
349 . <https://doi.org/10.1029/91JA01103>
- 350 Perez, J. K., & Northrop, T. G. (1970). Stationary waves produced by the earth's bow shock. *Jou*  
351 *rnal of Geophysical Research*, *75*(31), 6011-6023.  
352 <https://doi.org/10.1029/JA075i031p06011>
- 353 Ruhunusiri, S., Halekas, J. S., Espley, J. R., Eparvier, F., Brain, D., Mazelle, C., & Sulaiman, A.  
354 H. (2018). One-hertz waves at Mars: MAVEN observations. *Journal of Geophysical Researc*  
355 *h: Space Physics*, *123*(5), 3460-3476. <https://doi.org/10.1029/2017JA024618>

- 356 Russell, C. T., & Farris, M. H. (1995). Ultra low frequency waves at the Earth's bow shock. *Advances in Space Research*, 15(8-9), 285-296. [https://doi.org/10.1016/0273-1177\(94\)00108-D](https://doi.org/10.1016/0273-1177(94)00108-D)
- 357
- 358 Russell, C. T. (2007). Upstream whistler-mode waves at planetary bow shocks: A brief review. *Journal of atmospheric and solar-terrestrial physics*, 69(14), 1739-1746. <https://doi.org/10.1016/j.jastp.2006.11.004>
- 359
- 360
- 361 Sarantos, M., & Slavin, J. A. (2009). On the possible formation of Alfvén wings at Mercury during encounters with coronal mass ejections. *Geophysical research letters*, 36(4). <https://doi.org/10.1029/2008GL036747>
- 362
- 363
- 364 Slavin, J. A., & Holzer, R. E. (1981). Solar wind flow about the terrestrial planets 1. Modeling bow shock position and shape. *Journal of Geophysical Research: Space Physics*, 86(A13), 11401-11418. <https://doi.org/10.1029/JA086iA13p11401>
- 365
- 366
- 367 Slavin, J. A., DiBraccio, G. A., Gershman, D. J., Imber, S. M., Poh, G. K., Raines, J. M., ... & Solomon, S. C. (2014). MESSENGER observations of Mercury's dayside magnetosphere under extreme solar wind conditions. *Journal of Geophysical Research: Space Physics*, 119(10), 8087-8116. <https://doi.org/10.1002/2014JA020319>
- 368
- 369
- 370
- 371 Slavin, J. A., Middleton, H. R., Raines, J. M., Jia, X., Zhong, J., Sun, W. J., ... & Mays, M. L. (2019). MESSENGER observations of disappearing dayside magnetosphere events at Mercury. *Journal of Geophysical Research: Space Physics*, 124(8), 6613-6635. <https://doi.org/10.1029/2019JA026892>
- 372
- 373
- 374
- 375 Sonnerup, B. Ö., & Cahill Jr, L. J. (1967). Magnetopause structure and attitude from Explorer 12 observations. *Journal of Geophysical Research*, 72(1), 171-183. <https://doi.org/10.1029/JZ072i001p00171>
- 376
- 377
- 378 Sulaiman, A. H., Gurnett, D. A., Halekas, J. S., Yates, J. N., Kurth, W. S., & Dougherty, M. K. (2017). Whistler mode waves upstream of Saturn. *Journal of Geophysical Research: Space Physics*, 122(1), 227-234. <https://doi.org/10.1002/2016JA023501>
- 379
- 380
- 381 Tidman, D. A., & Krall, N. A. (1971). *Shock Waves in Collisionless Plasmas* (New York: Wiley Interscience). and, 151, 135.
- 382
- 383 Wilson, L. B. (2016). Low frequency waves at and upstream of collisionless shocks. *Washington DC American Geophysical Union Geophysical Monograph Series*, 216, 269-291. <https://doi.org/10.1002/9781119055006.ch16>
- 384
- 385
- 386 Winslow, R. M., Anderson, B. J., Johnson, C. L., Slavin, J. A., Korth, H., Purucker, M. E., ... & Solomon, S. C. (2013). Mercury's magnetopause and bow shock from MESSENGER Magnetometer observations. *Journal of Geophysical Research: Space Physics*, 118(5), 2213-2227. <https://doi.org/10.1002/jgra.50237>
- 387
- 388
- 389
- 390 Winslow, R. M., Lugaz, N., Philpott, L. C., Schwadron, N. A., Farrugia, C. J., Anderson, B. J., & Smith, C. W. (2015). Interplanetary coronal mass ejections from MESSENGER orbital observations at Mercury. *Journal of Geophysical Research: Space Physics*, 120(8), 6101-6118. <https://doi.org/10.1002/2015JA021200>
- 391
- 392
- 393
- 394 Winslow, R. M., Philpott, L., Paty, C. S., Lugaz, N., Schwadron, N. A., Johnson, C. L., & Korth, H. (2017). Statistical study of ICME effects on Mercury's magnetospheric boundaries and nor
- 395

- 396       thern cusp region from MESSENGER. *Journal of Geophysical Research: Space Physics*, 122(  
397       5), 4960-4975. <https://doi.org/10.1002/2016JA023548>
- 398       Winslow, R. M., Lugaz, N., Philpott, L., Farrugia, C. J., Johnson, C. L., Anderson, B. J., ... & Al  
399       Asad, M. (2020). Observations of extreme ICME ram pressure compressing Mercury's daysid  
400       e magnetosphere to the surface. *The Astrophysical Journal*, 889(2), 184. [https://iopscience.iop.  
401       org/article/10.3847/1538-4357/ab6170/meta](https://iopscience.iop.org/article/10.3847/1538-4357/ab6170/meta)
- 402       Zhong, J., Lee, L. C., Wang, X. G., Pu, Z. Y., He, J. S., Wei, Y., & Wan, W. X. (2020). Multiple  
403       X-line reconnection observed in Mercury's magnetotail driven by an interplanetary coronal m  
404       ass ejection. *The Astrophysical Journal Letters*, 893(1), L11. [https://iopscience.iop.org/article/1  
405       0.3847/2041-8213/ab8566/meta](https://iopscience.iop.org/article/10.3847/2041-8213/ab8566/meta)